Silver Nanoclusters | Hot Paper

How to cite: *Angew. Chem. Int. Ed.* **2022,** *61,* e202206742
International Edition: doi.org/10.1002/anie.202206742
German Edition: doi.org/10.1002/ange.202206742

An Ultrastable 155-Nuclei Silver Nanocluster Protected by Thiacalix[4]arene and Cyclohexanethiol for Photothermal Conversion

*Zhi Wang, Fahri Alkan, Christine M. Aikens, Mohamedally Kurmoo, Zhen-Yi Zhang, Ke-Peng Song, Chen-Ho Tung, and Di Sun**

Abstract: Thiacalix[4]arenes have emerged as a family of macrocyclic ligands to protect metal nanoparticles, but it remains a great challenge to solve the mystery of their structures at the atomic level, especially for those larger than 2 nm. Here, we report the largest known mixed-valence silver nanocluster $[Ag_{155}(CyS)_{40}(TC4A)_5Cl_2]$ (**Ag155**) protected by deprotonated cyclohexanethiol (CySH) and macrocyclic ligand *p-tert*-butylthiacalix[4]arene (H_4TC4A). Its single-crystal structure consists of a metallic core of four concentric shells, $Ag_{13}@Ag_{42}@Ag_{30}@Ag_{70}$, lined with a organic skin of $40CyS^-$ and $5TC4A^{4-}$ and $2Cl^-$. **Ag155** manifests an unusual pseudo-5-fold symmetry dictated by the intrinsic metal atom packing and the regioselective distribution of mixed protective ligands. This work not only reveals a macrocyclic ligand effect on the formation of a large silver nanocluster, but also provides a new structural archetype for comprehensively perceiving their interface and metal kernel structures.

Introduction

Silver nanoclusters have gained increasing attention in terms of their aesthetic structures alongside their promising applications in catalysis, biomedicine, chemical sensing, and biolabeling.[1] The atomically-precise elucidation of silver nanocluster structures in the transition size around 2 nm is the overarching goal to understand the quantum size effect and structure–property correlations.[2] Nonetheless, the synthesis and crystallization of silver nanoclusters remain laborious trial-and-error processes so that structures of clusters around 2 nm in size have rarely been reported.[3] To date, only a few atomically-precise structures of ≈2 nm silver nanoclusters are known including Ag_{100}, Ag_{136}, Ag_{141}, Ag_{146}, Ag_{180}, Ag_{206}, Ag_{210}, Ag_{211}, and Ag_{374}, which are mostly protected by thiol ligands because of the ease of formation of the robust Ag–S bond.[4] In an effort to surmount the synthetic obstacle, a myriad of ligands, e.g. thiol, alkyne, phosphine, amido and their combinations, have been used for the protective monolayer; furthermore, some universal synthetic strategies, e.g. seed growth, anion template, amine-assisted $NaBH_4$ reduction have been employed to allow silver nanocluster chemistry to blossom.[5] These ligands with some rigidity form diverse interface motifs to protect the silver nanoclusters and also contribute largely to the growth of their single crystals for subsequent crystallographic characterizations. Beyond these conventional ligands, macrocyclic ligands are promising candidates for the construction of polynuclear metal compounds by virtue of their preinstalled multidentate coordination sites;[6] however, they markedly lag behind in protecting coinage metal nanoclusters.

Based on the synergistic multidentate chelating effect, one famous family of macrocyclic ligands, *p-tert*-butylthiacalix[4]arene (H_4TC4A), composed of phenolic hydroxyl and bridging sulfur groups in proximity of each other, have been employed to construct polyhedral coordination cages.[7] Awareness of the potential of some macrocyclic organics acting as passivation ligands for metal nanoclusters has been raised only very recently, such as the attempts to install phosphine-calixarene and tetrathiolate-calixarene on gold nanoclusters.[8] Unfortunately, due to their difficult crystallizing nature hampering single-crystal X-ray diffraction (SCXRD), their compositions and structures have to be consequently deduced from electrospray ionization mass spectrometry (ESI-MS) and nuclear magnetic resonance spectroscopy (NMR) combined with density functional theory (DFT) calculations.

In spite of the difficulty in crystallization of metal clusters protected by only $TC4A^{4-}$, the combination of this bulky one with some small auxiliary ligands may open the door to high-quality crystalline products of silver nanoclusters, which, in turn, helps us to understand in detail their molecular and electronic structures.[9] In this scenario, some

---

[*] Z. Wang, K.-P. Song, C.-H. Tung, Prof. D. Sun
School of Chemistry and Chemical Engineering,
State Key Laboratory of Crystal Materials, Shandong University
Ji'nan, 250100 (P. R. China)
E-mail: dsun@sdu.edu.cn

Prof. F. Alkan
Department of Nanotechnology Engineering,
Abdullah Gül University
Kayseri (Turkey)

Prof. C. M. Aikens
Department of Chemistry, Kansas State University
Manhattan, KS 66506 (USA)

Prof. M. Kurmoo
Institut de Chimie de Strasbourg,
Université de Strasbourg, CNRS-UMR 7177
4 rue Blaise Pascal, 67008 Strasbourg Cedex (France)

Dr. Z.-Y. Zhang
Bruker (Beijing) Scientific Technology Co., Ltd. (P. R. China)

efforts have been devoted to explore the assembly and crystallization conditions of macrocycle ligand-protected silver nanoclusters in the presence of small thiolate or alkyne ligands. The use of macrocyclic ligands to protect metal nanoclusters has been slowly evolving from academic curiosity with poorly identified species to become a synthetic reality by the pioneering work of Wang et al. who reported the first structurally determined thiacalixarene protected Ag_{35} nanocluster.[10] The monolayer of ligands consists of thiacalixarene and $^{t}BuC{\equiv}C^{-}$ distributed to two concentrated regions of the Ag_{35} cluster. Very recently, we have presented the synthesis and structural characterization of a C_4-symmetric Ag_{88} "super calix" constructed from eight Ag_{11} secondary building units encircling a CrO_4^{2-} template at the core.[11] That is the highest-nuclearity metal cluster based on $TC4A^{4-}$ ever reported. Furthermore, we also noted the importance of auxiliary small ligands in this structure that can fill the space between the bulky $TC4A^{4-}$ through the naked silver atoms at the surface. They also play an important role to stabilize the overall electronics and geometry of the metal nanoclusters. From these sporadic reports, we found that large-sized silver nanoclusters (>100 metal atoms) protected by the $TC4A^{4-}$ ligand are not yet available. Thus, more efforts are urgently needed to unravel certain chemical fundamentals (e.g. metal atom packing, metal-ligand interfacial motif, ligand distribution on the surfaces and so on) of metal nanoclusters protected by such macrocyclic ligand.

Given the above considerations, herein, a 155-nuclei silver nanocluster $[Ag_{155}(CyS)_{40}(TC4A)_5Cl_2]$ (CySH = cyclohexanethiol; **Ag155**) was successfully synthesized and fully characterized by X-ray crystallography, UV/Vis spectroscopy and ESI-MS. This peculiar nanocluster i) is the first structurally determined silver-TC4A nanocluster with a core size close to 2 nm; ii) has a novel structure consisting of four concentric shells forming an onion-like $Ag_{13}@Ag_{42}@Ag_{30}@Ag_{70}$ kernel; iii) displays pseudo 5-fold symmetry with mixed $TC4A^{4-}$ and CyS^{-} ligands showing regioselective coverage on the surface of metal core. This work delivers important insight about the novel metal-TC4A interface and multi-shell metal core structure.

Results and Discussion

The synthesis of **Ag155** involving the one-pot reduction of $(CySAg)_n$ and $AgNO_3$ in the presence of H_4TC4A and Et_3N by $NaBH_4$ at room temperature is described in Scheme 1 (see details in Supporting Information). Briefly, $(CySAg)_n$ and $AgNO_3$ were mixed together in $^{n}BuOH$ followed by a $CHCl_3$ solution of H_4TC4A. Subsequently, a freshly prepared ethanolic solution of $NaBH_4$ was added dropwise under vigorous stirring and followed by the addition of Et_3N. The resulting white turbid solution gradually turned to brown and then black. Finally, the reaction mixture was aged for 6 h in the dark. The solution was filtered, and single crystals of **Ag155** suitable for X-ray diffraction were obtained by slow evaporation of the filtrate for three months. Of note, neither other laboratory-available silver salts nor alcohols other than $^{n}BuOH$ work in this system. Other weaker reducing agents such as Ph_2SiH_2 and $NaBH_3CN$ were also tried in this system but **Ag155** cannot be isolated. Nevertheless, the reproducibility of **Ag155** is very well at the same experiment conditions.

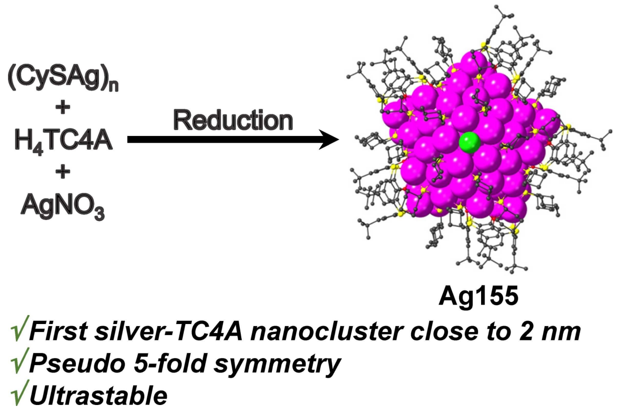

Scheme 1. Synthesis route for **Ag155**. CySH = cyclohexanethiol, H_4TC4A = *p-tert*-butylthiacalix[4]arene.

SCXRD analyses revealed that **Ag155** crystallized in the triclinic space group $P\bar{1}$ (No. 2) with a composition of $[Ag_{155}(CyS)_{40}(TC4A)_5Cl_2]$.[12] Based on the X-ray crystallography, we did not directly identify any counter-anions due to their highly disordered orientations in the lattice, but the vibrational bands in infrared ($\nu_3 = 1306\ cm^{-1}$) and Raman ($\nu_1 = 1005\ cm^{-1}$) spectra clearly proved the counter-anion to be NO_3^- (Figure S1).[13] Two complete molecules related by the inversion center are packed together per unit cell. An asymmetric unit consists of a complete cluster with a kernel of 155 independent Ag atoms wrapped by $5\,TC4A^{4-}$, $40\,CyS^{-}$ and $2\,Cl^{-}$ (Figure 1). The axial thickness and equatorial diameter of the **Ag155** kernel are 1.3 and 1.7 nm, respectively. The overall morphology of **Ag155** looks like a titoni and the entire **Ag155** exhibits pseudo-C_{5h} symmetry.

For a more detailed dissection of the kernel structure, as illustrated in Figure 2, the arrangement of the 155 silver atoms resembles an onion that can be peeled as four shells $Ag_{13}@Ag_{42}@Ag_{30}@Ag_{70}$ from inner to outer. All four shells share the same C_5 axis passing through two Cl atoms at two poles. In the innermost shell of the cluster is a 13-silver-atom Ino decahedron (1st shell, Figure 2a and e), which is built from two Ag_7 pentagonal bipyramids in an eclipsed conformation through sharing vertices. The Ag⋯Ag distances in Ag_{13} fall in a range of 2.80–2.88 Å (Table S1), which is in agreement with the distances in related silver nanoclusters and almost the same to those in silver metal.[14] This Ag_{13} shell is caged by an Ag_{42} shell (2nd shell), producing a double-shell Ag_{55} Ino decahedron. The Ag_{42} shell is an intermediate between the 5-fold symmetric Ag_{32} shell in Ag_{206}[4f] and the Ag_{52} shell in Ag_{210},[4g] which is mandated by the heights of their 1st shell (Figure S2). The Ag⋯Ag distances in 2nd shell are in the range 2.81–3.05 Å (Table S2). This kind of M_{55} Ino decahedron with ten (111) facets at two poles and five (100) facets at the equator is an isomer of the M_{55} Mackay icosahedron observed in Ag_{112} and Au_{133} (Fig-

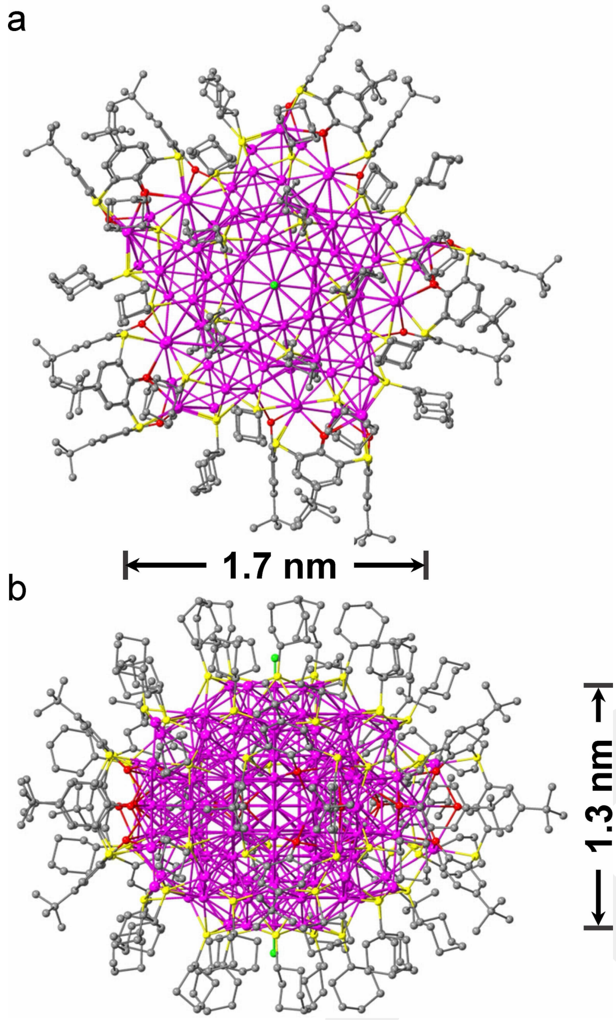

Figure 1. Structure of **Ag155**: Top (a) and side (b) views. The molecular dimensions were measured without considering the ligand shell. Color labels: Purple, Ag; yellow, S; green, Cl; gray, C; red, O.

ure S3).[15] The 3rd Ag_{30} shell is an opened pentagonal prism (Figure 2c and g), which is made up of two face-to-face Ag_{15} pentagons. This Ag_{30} shell is a reduced version of the pentagonal prism in Ag_{210} (Figure S4) and the average Ag···Ag distance is 2.95 Å (Table S3).[4g] The three-shelled Ag_{85} is enclosed by the outer Ag_{70} semi-closed shell that is formed by two Ag_{25} cupolas (pink in Figure 2d and h) at the polar sites connecting to five Ag_4 folded rhombuses (purple in Figure 2d and h) evenly distributed at the equatorial belt ($25\times2+4\times5=70$). The Ag···Ag distances in 4th shell are around 2.82–3.52 Å (Table S4). This Ag_{25} cupola consists of one pentagon, five tetragons and fifteen trigons (Figure S5). Alternatively, it can be seen as ten silver atoms appending on the periphery of a half of a pentagonal cupola (J_5, one of Johnson solids) by sharing the alternate edges of silver trigons and tetragons.[16] There is a C_5 axis passing through two Cl atoms at the top/bottom poles and a horizontal symmetry-plane at the equator of **Ag155** (Figure S6). Due to the absence of a C_2 axis perpendicular to the C_5 axis, the whole symmetry point group is C_{5h} rather than common D_{5h}. The average Ag···Ag distances between the 1st and 2nd, 2nd and 3rd, 3rd and 4th shells are 2.88, 2.88, and 2.97 Å, respectively (Table S5, Figure S7).

The kernel of the silver nanoparticle is further shielded by a mixture of ligands comprised of $5\,TC4A^{4-}$, $40\,CyS^{-}$ and $2\,Cl^{-}$. Five $TC4A^{4-}$ can be classified into the three types on the basis of their coordination modes (Figure 3a):

two of μ_7-$\kappa_o^{\,4} : \kappa_o^{\,3} : \kappa_o^{\,3} : \kappa_o^{\,3} : \kappa_s^{\,1} : \kappa_s^{\,1} : \kappa_s^{\,1} : \kappa_s^{\,1}$,

two of μ_7-$\kappa_o^{\,4} : \kappa_o^{\,3} : \kappa_o^{\,3} : \kappa_o^{\,2} : \kappa_s^{\,1} : \kappa_s^{\,1} : \kappa_s^{\,1} : \kappa_s^{\,1}$,

one of μ_6-$\kappa_o^{\,3} : \kappa_o^{\,3} : \kappa_o^{\,3} : \kappa_o^{\,3} : \kappa_s^{\,1} : \kappa_s^{\,1} : \kappa_s^{\,1} : \kappa_s^{\,1}$

Each $TC4A^{4-}$ not only bound to the Ag_4 folded rhombus on the equatorial belt but also ride on the vertical edge of Ag_{30} pentagonal prism (Figure 3b and c). Their bridging sulfur and phenolic oxygen atoms coordinate to Ag to consolidate the outmost and sub-outmost silver shells with Ag–S and Ag–O bond lengths falling within the ranges of 2.53–2.71 and 2.2–2.8 Å, respectively. Different from previously reported Ag_{34},[17] Ag_{35}[10] and Ag_{88},[11] the silver atom sitting in the center of the $TC4A^{4-}$ in **Ag155** is coordinated by only three phenolic oxygen atoms, forming seven bonds with silver atoms. The one remaining phenolic oxygen atom is far away from the other three and bound to three or four silver atoms (cyan ball in Figure 3a) in the Ag_{30} shell. Owing to the asymmetrical distributions of silver atoms in the lower rim of $TC4A^{4-}$, each of them exhibits a distorted configuration with the dihedral angles in the range of 74–139° between the phenyl rings and the plane defined by four oxygen atoms.

Apart from the five $TC4A^{4-}$, there are $40\,CyS^{-}$ on the surface. Among them, thirty are bisected to cap on two Ag_{25} cupolas up and down, whereas the remaining ten are inserted into the interstices between two adjacent $TC4A^{4-}$ on the equatorial belt. The CyS^{-} exhibit two types of bonding motifs, 16 μ_3 and 24 μ_4, towards silver atoms with the Ag–S bond lengths ranging from 2.39 to 2.96 Å (Figure 4a). As portrayed in Figure 4b and c, the CyS^{-} on the equatorial belt not only ligate to the Ag_4 folded rhombus but also interact with partial silver atoms of the Ag_{30} shell. Because of the regioselective distribution of $TC4A^{4-}$ and CyS^{-} at the equatorial belt, the shape of the **Ag155** resembles a titoni. To complement the coordination vacancy on the silver kernel, two Cl^{-} ions are found to stand on the vertices of the Ag_{42} shell with an average Ag–Cl bond length of 2.64 Å. Upon scrutinization of the synthesis raw material, the Cl^{-} is likely formed by the cleavage of the C–Cl bond of $CHCl_3$.[18] To the best of our knowledge, **Ag155** is the largest silver nanocluster protected by $TC4A^{4-}$.

ESI-MS has been implemented as an effective method to verify the composition and assembly mechanism of metal nanoclusters in the realm of cluster chemistry.[19] Therefore, the ESI-MS of **Ag155** dissolved in $CHCl_3$ was performed in both positive and negative ion modes. No informative signal was detected in the negative-ion mode, but one envelope centered at m/z 12492.242 (**1a**) was observed in positive ion mode with the pre plus storage time of 90 μs (Figure 5a). Its

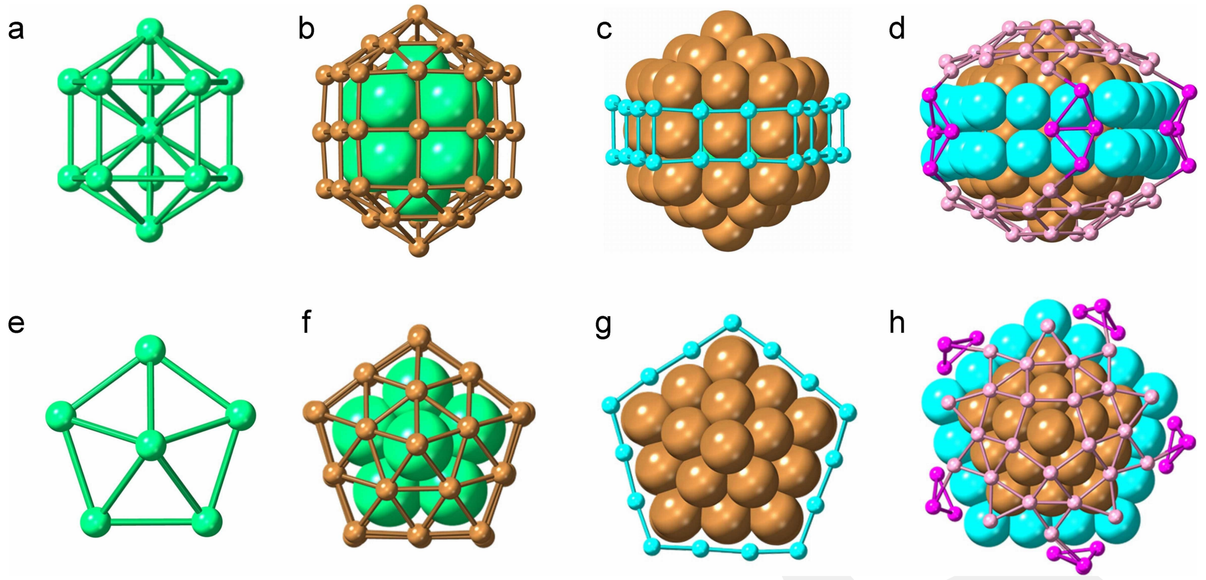

Figure 2. Side and top views of the structure dissection of **Ag155** kernel. a), e) The 1st Ag_{13} shell (green); b), f) The 2nd Ag_{42} shell (brown); c), g) The 3rd Ag_{30} shell (cyan); d), h) The 4th Ag_{70} shell (pink and purple).

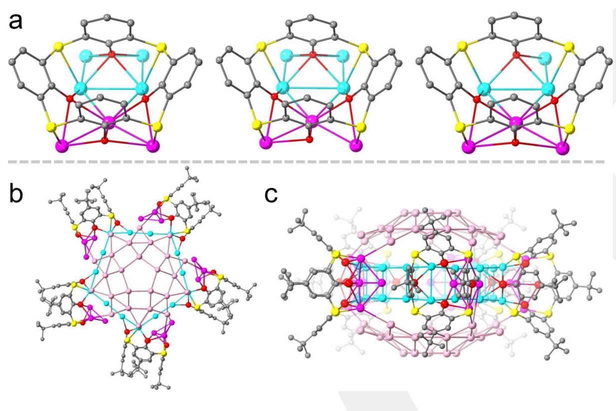

Figure 3. a) The surface motifs formed between $TC4A^{4-}$ and silver atoms. The tert-butyl groups were removed for clarity. Top (b) and side (c) views of the $TC4A^{4-}$ ligands bridging the outermost and sub-outermost silver shells. Color labels: Purple, pink and cyan, Ag; yellow, S; gray, C; red, O.

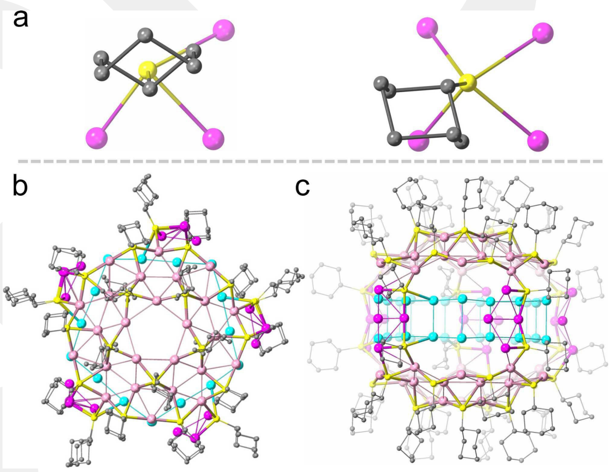

Figure 4. a) The surface motifs formed between CyS^- and silver atoms. Top (b) and side (c) views of the CyS^- ligands bridging the outermost and sub-outermost silver shells. Color labels: Purple, pink and cyan, Ag; yellow, S; gray, C.

charge state, determined by the separation of isotope peaks, is +2. After careful comparison of experimental and simulated isotopic envelopes, its composition is exactly assigned to $[Ag_{155}(CyS)_{40}(TC4A)_5Cl_2]^{2+}$ (calcd. 12492.296), which matches well with the formula determined by X-ray crystallography, indicating its high stability in $CHCl_3$.

What is more fascinating is that an envelope was additionally detected at m/z 8328.165 (**1b**) when the pre plus storage time parameter was shortened from 90 to 70 μs (Figure 5b). The peak belongs to a +3 species which perfectly agrees with $[Ag_{155}(CyS)_{40}(TC4A)_5Cl_2]^{3+}$ (calcd. 8328.197). Generally speaking, the pre plus storage is a decay for collecting ions between the transfer time and time of flight pulser on. The shorter pre plus storage time facilitates the transfer of lighter ions to the detector, which is consistent with the phenomenon we observed above.

In addition to $CHCl_3$, **Ag155** can also be dissolved in EtOH and the ESI-MS of **Ag155** in EtOH shows two similar envelopes **1a′** (exp. 12492.077) and **1b′** (exp. 8328.070) in the m/z range of 5000–15000 to those in $CHCl_3$ but with different abundances (Figure S8), which demonstrated that **Ag155** also remains integrity in ethanol.

The high-angle annular dark-field scanning transmission electron microscopy (HAADF-STEM) images taken in three different regions show a high degree of homogeneity of the nanoparticles in both size and shape. The measured average diameters of nanoparticles are 1.324±0.083, 1.337±0.110 and 1.308±0.041 nm, respectively, consistent with the pole-to-pole distance (1.3 nm) of **Ag155** determined by SCXRD (Figure S9). Nonspherical **Ag155**, capped by the

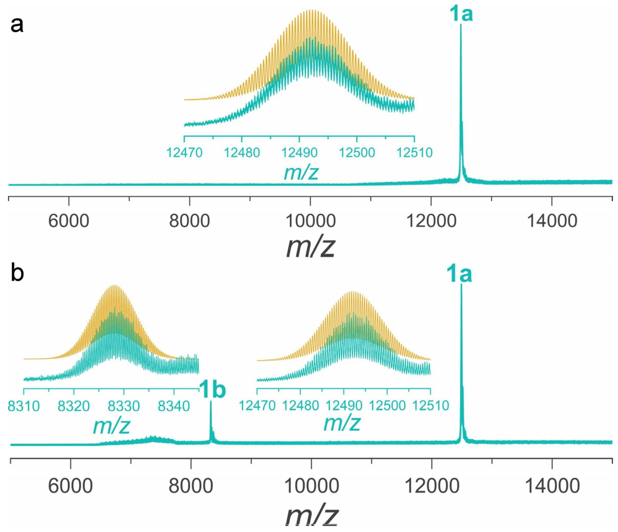

Figure 5. Positive-ion mode ESI-MS of **Ag155** dissolved in $CHCl_3$ with different pre plus storage time parameters: a) 90 μs and b) 70 μs. Insets: The experimental (blue lines) and simulated (yellow lines) isotope-distribution patterns of **1a** and **1b**.

anisotropic arrangement of surface ligands, $TC4A^{4-}$ and CyS^-, shows such a homogeneous size under the TEM, which suggests that they may align on carbon substrate with a unified orientation, dictated by interfacial energy mainly involving hydrophobic interactions at the interface between the carbon substrate and nanocluster. Combing with above ESI-MS results, we can conclude that **Ag155** is highly stable in both $CHCl_3$ and ethanol, even under the ESI-MS condition and low-dose electron beam bombardment. Furthermore, **Ag155** in the solid state can keep stable for at least one year under ambient environment and below 110 °C under thermal treatment, as revealed by IR, TGA and variable temperature PXRD, respectively (Figure S10 and S11).

The UV/Vis spectrum of **Ag155** was acquired in the wavelength range 300–900 nm (Figure 6). A pronounced peak was observed at 460 nm, consistent with the surface plasmon bands of the silver nanoclusters of size reaching close to 2 nm.[4b,c,d,g] Moreover, it can preserve stable in $CHCl_3$ for at least one month at room temperature (Figure S12). Such high stability also implies the closed-shell electronic configuration of **Ag155**. Although we found the dominant species to be doubly charged, such as $[Ag_{155}(CyS)_{40}(TC4A)_5Cl_2]^{2+}$, no signal was detected in the electron spin resonance (ESR) spectrum (Figure S13), which suggests that even number of free electrons should exist in **Ag155**. Therefore, the genuine formula of **Ag155** should be $[Ag_{155}(CyS)_{40}(TC4A)_5Cl_2]^+$, with a single NO_3^- ion. The changed charge state of metal nanoclusters during ESI process is assigned to charge stripping and has been widely observed in several other cases such as Ag_{11} and Ag_{17}.[5d,20] The monocationic Ag_{155} possesses 92 free valence electrons ($92 = 155\ (Ag) - 20\ (TC4A) - 40\ (CyS) - 2(Cl) - 1(z)$) with a delocalized superatomic orbital filling written as $1S^2|1P^6|1D^{10}|2S^21F^{14}|2P^61G^{18}|2D^{10}3S^21H^{22}$.[21] This shell-closing electron count falls in the "magic" number series (2, 8, 18, 34, 58, 92),[22] so **Ag155** is expected to be an electron shell closing system. Moreover, we also ruled out the possibility of **Ag155** being a hydride by using the $NaBD_4$ as reductant in the synthesis. The as-obtained crystals exhibit the similar unit cell parameters in SCXRD and envelope in ESI-MS experiment (Figure S8).

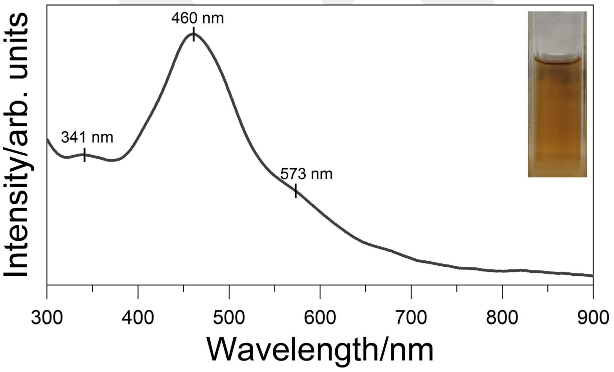

Figure 6. The ultraviolet-visible absorption spectrum of **Ag155** recorded in $CHCl_3$ at room temperature. Inset: photograph of **Ag155** solution.

To further understand the electronic structure of **Ag155**, we performed DFT calculations. We note that the calculations on **Ag155** with different charge states ($q = -1$, $+2$, -2) result with somewhat problematic self-consistent field (SCF) convergence due to energetically close occupied-unoccupied levels, whereas $q = +1$ case for the cluster results with a HOMO–LUMO gap of 0.41 eV, and smooth SCF convergence. This is related to the previously discussed shell-closing electron count for **Ag155** cluster with +1 charge, which is also supported by DFT results. In Figure 7a, we show the partial and total density of states (DOS) curves for the model $[Ag_{155}(SH)_{40}(TC4A)_5Cl_2]^{1+}$ cluster (abbreviated as Ag_{155} in this section, Figure S14). The HOMO–LUMO gap is calculated to be 0.41 eV. Partial DOS curves show that atomic Ag *s* and *p* orbitals largely contribute to the low-lying occupied and unoccupied levels of the cluster. The *p* orbitals of S, O and C also contribute to the low-lying occupied levels considerably, whereas their contribution to the unoccupied levels is somewhat smaller. Total DOS curve exhibits an intense feature for the −8 to −12 eV energy range of the electronic structure, which mainly originates from the Ag *d* band as seen from the partial DOS curves and energy levels.

In Figure 7b, we show the calculated UV/Vis spectrum for the Ag_{155} cluster, along with the stick spectrum that only shows transitions with oscillator strengths larger than 0.02. Overall, the calculated spectrum shows a good agreement with the experimental spectrum shown in Figure 6. The main feature in the theoretical spectrum is an intense peak around 2.9 eV. As shown in the stick spectrum, this feature originates from several closely-spaced transitions. It should be noted that the energy and the origin of this peak is quite similar to the plasmonic peak from the recently investigated Ag_{211} cluster.[4g] In addition to the intense feature at 2.9 eV, the spectrum of the Ag_{155} cluster also exhibits a shoulder

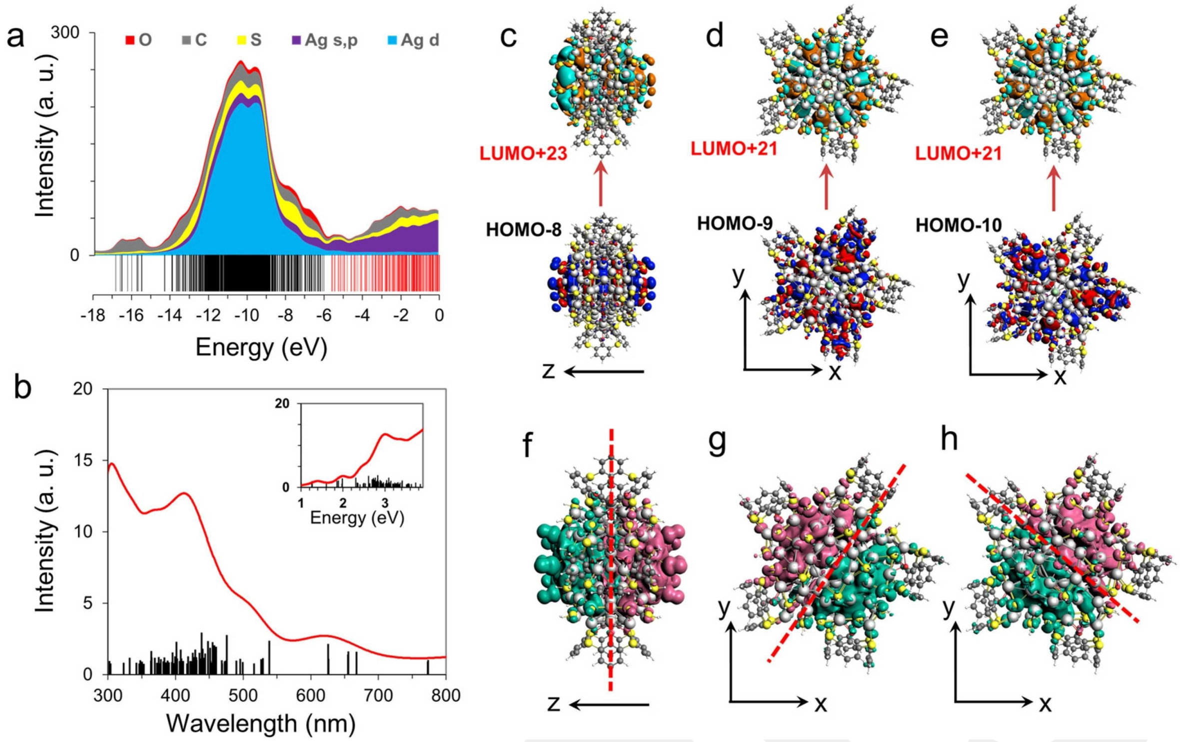

Figure 7. a) Partial and total DOS curves of the Ag_{155} cluster. b) Calculated UV/Vis spectrum (red) and the stick spectrum of excited states with oscillator strengths larger than 0.02 a.u. (black). c) Illustration of occupied and unoccupied molecular orbitals for HOMO-8→LUMO+23 transition. d) Occupied and unoccupied molecular orbitals for HOMO-9→LUMO+21 transition. e) Occupied and unoccupied molecular orbitals for HOMO-10→LUMO+21 transition. f) TFD of the excited state resulting from the constructive coupling of configurations with transition-dipole moment along the C_5 axis. g) and h) TFD of the excited state resulting from the constructive coupling of configurations with transition-dipole moment orthogonal to the unique C_5 axis.

around 2.5 eV and a broad peak centered around 2.0 eV. Unlike the peak at 2.9 eV, these features mainly originate from a small number of scattered transitions.

In Figure 7c–e, we show the occupied→unoccupied pairs with the largest oscillator strengths for the Ag_{155} cluster. As seen from the figure, these orbitals mainly originate from the Ag *s* and *p* band of the electronic structure. The HOMO−8→LUMO+23 transition (Figure 7c) exhibits the largest oscillator strength among the possible transitions. The nodes of both orbitals lie on the unique C_5 axis (z) of the cluster, which results in a transition-dipole moment along this axis. In comparison, transition-dipole moments (*x*, *y*) of HOMO-9→LUMO+21 (Figure 7d) and HOMO-10→LUMO+21 (Figure 7e) transitions are orthogonal to the C_5 axis of the cluster.

To further understand the origin of spectral features, we perform a restricted TDDFT+TB excited-state calculation where only the occupied→unoccupied pairs with oscillator strengths larger than 0.5 are included in the configuration interaction (CI). As a result of this restriction, the CI space is reduced to only 16 configurations, which greatly simplifies our analysis. Detailed excited state information of selective states is given in Table S7. From the results of this analysis, it is seen that constructive coupling of high-oscillator-strength configurations, which exhibit a transition-dipole moment along the C_5 axis, result in an excited state at 2.80 eV. The transition-fit density (TFD) of this excited state shows a large dipole along the C_5 axis as shown in Figure 7f. In comparison, constructive coupling of configurations with a transition-dipole moment orthogonal to the C_5 axis results in two approximately degenerate excited states at 1.95 eV. Similarly, TFDs exhibit a large dipole orthogonal to the C_5 axis as shown in Figure 7g and h. We note that the energies of these excited states agree well with the energies of spectral features shown in Figure 7b. These results show that the constructive coupling of these configurations with transition-dipole moments along the C_5 axis primarily contribute to the intense peak at ≈2.9 eV (Figure 7b), whereas configurations with transition-dipole moments orthogonal to the C_5 axis mostly contribute to the peak at ≈2.0 eV.

Based on such atom-precise structure, we further explored if it can induce an intense photothermal effect. First of all, **Ag155** was dissolved in chloroform with different concentrations ranging from 60 to 240 μM, and then irradiated with a 660 nm laser at the low power density of 100 $mW\,cm^{-2}$. As shown in Figure 8a, the temperatures of them all increase under the laser irradiation, indicating **Ag155** possess the ability of photothermal conversion. The temperatures are proportional to the **Ag155** concentrations, which are all reached their plateaus at 41.4, 53.9 and 59.1 °C within 300 s, respectively (Figure 8b). The maximum tem-

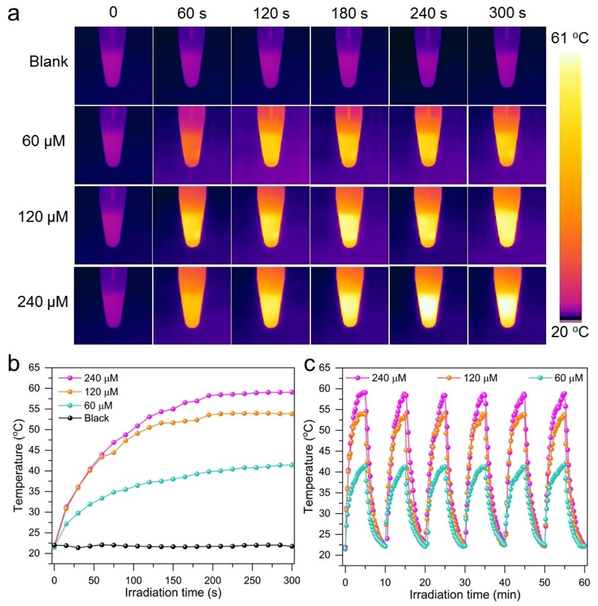

Figure 8. a) IR thermal images recorded with a thermal imaging camera at different irradiation times. b) Plots of temperature rise of different concentrations of **Ag155** solution and blank solvent with time. c) Photothermal heating and natural cooling cycles under 660 nm laser irradiation with power density of 100 mW cm^{-2}.

peratures are almost constant without significant attenuation in 6 cycles heating and cooling processes (Figure 8c). Furthermore, the compared UV/Vis spectra of **Ag155** before and after irradiation verified the excellent photothermal stability of the nanocluster (Figure S15). No obvious temperature fluctuation ($t < 1\,°C$) was detected in blank chloroform, corroborating that the temperature variations under the laser irradiation are all contributed by **Ag155**. A dramatic temperature increase from 20 to 59.1 °C is observed within 300 s irradiation, which is found to be much better than those of some common materials reported in the literature, such as azobenzene derivatives and nanobioconjugates.[23] This is mainly because no fluorescence is observed in **Ag155** under the irradiation of 660 nm, suggesting very weak radiative migration. Therefore, photothermal conversion become the overriding route of energy release.

Conclusion

To summarize, an unprecedented 155-nuclei silver nanocluster was synthesized and its structure was determined by X-ray crystallography. It is a multishell structure consisting of a concentric $Ag_{13}@Ag_{42}@Ag_{30}@Ag_{70}$ kernel protected by $5\,TC4A^{4-}$, $40\,CyS^{-}$ and $2\,Cl^{-}$. As the largest silver nanocluster based on the macrocyclic thiacalix[4]arene ligand, **Ag155** exhibits pseudo 5-fold symmetry due to the regioselective coordination of $TC4A^{4-}$ and CyS^{-} on the surface of the silver nanocluster as well as the intrinsic metal atom packing. The successful incorporation of $TC4A^{4-}$ on this silver nanocluster paves a brand new avenue for the synthesis of large-sized silver nanoclusters and provides direct evidence to decipher the electronic and interface structures of silver nanoparticles.

Acknowledgements

This work was financially supported by the National Natural Science Foundation of China (Grant Nos. 22171164, 91961105, 21822107, 21827801), the Fok Ying Tong Education Foundation (171009). Z.W. acknowledges support from the National Postdoctoral Innovative Talents Support Program (No. BX2021171) and China Postdoctoral Science Foundation (No. 2021M700081). C.M.A. was supported by the National Science Foundation (CHE-1905048) of the United States. The computing for this project was performed on the Beocat Research Cluster at Kansas State University, which is funded in part by NSF grants CHE-1726332, CNS-1006860, EPS-1006860, and EPS-0919443. The computing for this project was performed on the HPC Research Cluster at Abdullah Gül University.

Conflict of Interest

The authors declare no conflict of interest.

Data Availability Statement

The data that support the findings of this study are available in the Supporting Information of this article.

Keywords: C_{5h} Symmetry · ESI-MS · Photothermal Conversion · Silver Nanocluster · Thiacalix[4]arenes

---

[1] a) J. Yan, B. K. Teo, N. Zheng, *Acc. Chem. Res.* **2018**, *51*, 3084–3093; b) X. Du, R. Jin, *ACS Nano* **2019**, *13*, 7383–7387; c) S. Sharma, K. K. Chakrahari, J.-Y. Saillard, C. W. Liu, *Acc. Chem. Res.* **2018**, *51*, 2475–2483; d) H. Yu, B. Rao, W. Jiang, S. Yang, M. Zhu, *Coord. Chem. Rev.* **2019**, *378*, 595–617; e) A. Schnepf, H. Schnoeckel, *Angew. Chem. Int. Ed.* **2014**, *53*, 3064–3066; *Angew. Chem.* **2014**, *126*, 3124–3127; f) R. J. Wilson, N. Lichtenberger, B. Weinert, S. Dehnen, *Chem. Rev.* **2019**, *119*, 8506–8554; g) Q. Yao, X. Yuan, T. Chen, D. T. Leong, J. Xie, *Adv. Mater.* **2018**, *30*, 1802751.

[2] a) N. Yan, N. Xia, L. Liao, M. Zhu, F. Jin, R. Jin, Z. Wu, *Sci. Adv.* **2018**, *4*, eaat7259; b) Z. Wu, Q. Yao, S. Zang, J. Xie, *ACS Mater. Lett.* **2019**, *1*, 237–248.

[3] K. Yonesato, H. Ito, H. Itakura, D. Yokogawa, T. Kikuchi, N. Mizuno, K. Yamaguchi, K. Suzuki, *J. Am. Chem. Soc.* **2019**, *141*, 19550–19554.

[4] a) X. Ma, Y. Bai, Y. Song, Q. Li, Y. Lv, H. Zhang, H. Yu, M. Zhu, *Angew. Chem. Int. Ed.* **2020**, *59*, 17234–17238; *Angew. Chem.* **2020**, *132*, 17387–17391; b) H. Yang, Y. Wang, X. Chen, X. Zhao, L. Gu, H. Huang, J. Yan, C. Xu, G. Li, J. Wu, A. J. Edwards, B. Dittrich, Z. Tang, D. Wang, L. Lehtovaara, H. Hakkinen, N. Zheng, *Nat. Commun.* **2016**, *7*, 12809; c) L. Ren, P. Yuan, H. Su, S. Malola, S. Lin, Z. Tang, B. K. Teo, H. Hakkinen, L. Zheng, N. Zheng, *J. Am. Chem. Soc.* **2017**, *139*, 13288–13291; d) Y. Song, K. Lambright, M. Zhou, K. Kirschbaum, J. Xiang, A. Xia, M. Zhu, R. Jin, *ACS Nano* **2018**, *12*,

9318–9325; e) Z. Wang, H.-F. Su, Y.-Z. Tan, S. Schein, S.-C. Lin, W. Liu, S.-A. Wang, W.-G. Wang, C.-H. Tung, D. Sun, L.-S. Zheng, *Proc. Natl. Acad. Sci. USA* **2017**, *114*, 12132–12137; f) J. Yan, J. Zhang, X. Chen, S. Malola, B. Zhou, E. Selenius, X. Zhang, P. Yuan, G. Deng, K. Liu, H. Su, B. K. Teo, H. Hakkinen, L. Zheng, N. Zheng, *Nat. Sci. Rev.* **2018**, *5*, 694–702; g) J.-Y. Liu, F. Alkan, Z. Wang, Z.-Y. Zhang, M. Kurmoo, Z. Yan, Q.-Q. Zhao, C. M. Aikens, C.-H. Tung, D. Sun, *Angew. Chem. Int. Ed.* **2019**, *58*, 195–199; *Angew. Chem.* **2019**, *131*, 201–205.

[5] a) Z. Lei, X.-K. Wan, S.-F. Yuan, Z.-J. Guan, Q.-M. Wang, *Acc. Chem. Res.* **2018**, *51*, 2465–2474; b) L. G. AbdulHalim, M. S. Bootharaju, Q. Tang, S. Del Gobbo, R. G. AbdulHalim, M. Eddaoudi, D.-e. Jiang, O. M. Bakr, *J. Am. Chem. Soc.* **2015**, *137*, 11970–11975; c) C. P. Joshi, M. S. Bootharaju, M. J. Alhilaly, O. M. Bakr, *J. Am. Chem. Soc.* **2015**, *137*, 11578–11581; d) A. Ghosh, M. Bodiuzzaman, A. Nag, M. Jash, A. Baksi, T. Pradeep, *ACS Nano* **2017**, *11*, 11145–11151; e) X. Liu, J. Chen, J. Yuan, Y. Li, J. Li, S. Zhou, C. Yao, L. Liao, S. Zhuang, Y. Zhao, H. Deng, J. Yang, Z. Wu, *Angew. Chem. Int. Ed.* **2018**, *57*, 11273–11277; *Angew. Chem.* **2018**, *130*, 11443–11447; f) S.-F. Yuan, Z.-J. Guan, W.-D. Liu, Q.-M. Wang, *Nat. Commun.* **2019**, *10*, 4032; g) Z. Wang, H.-F. Su, M. Kurmoo, C.-H. Tung, D. Sun, L.-S. Zheng, *Nat. Commun.* **2018**, *9*, 2094.

[6] a) Y. Fang, Y. Deng, W. Dehaen, *Coord. Chem. Rev.* **2020**, *415*, 213313; b) P. Neri, J. L. Sessler, M. X. Wang, *Calixarenes and Beyond*, Springer, Cham, **2016**; c) R. Kumar, Y. O. Lee, V. Bhalla, M. Kumar, J. S. Kim, *Chem. Soc. Rev.* **2014**, *43*, 4824–4870; d) W. Sliwa, C. Kozlowski, *Calixarenes and Resorcinarenes: Synthesis, Properties and Applications*, John Wiley&Sons, **2009**.

[7] a) M. Liu, W. Liao, C. Hu, S. Du, H. Zhang, *Angew. Chem. Int. Ed.* **2012**, *51*, 1585–1588; *Angew. Chem.* **2012**, *124*, 1617–1620; b) Y. Bi, X.-T. Wang, W. Liao, X. Wang, X. Wang, H. Zhang, S. Gao, *J. Am. Chem. Soc.* **2009**, *131*, 11650–11651; c) X. Hang, B. Liu, X. Zhu, S. Wang, H. Han, W. Liao, Y. Liu, C. Hu, *J. Am. Chem. Soc.* **2016**, *138*, 2969–2972; d) K. Su, F. Jiang, J. Qian, M. Wu, Y. Gai, J. Pan, D. Yuan, M. Hong, *Inorg. Chem.* **2014**, *53*, 18–20; e) K.-C. Xiong, F.-L. Jiang, Y.-L. Gai, D.-Q. Yuan, D. Han, J. Ma, S.-Q. Zhang, M.-C. Hong, *Chem. Eur. J.* **2012**, *18*, 5536–5540.

[8] a) N. de Silva, J.-M. Ha, A. Solovyov, M. M. Nigra, I. Ogino, S. W. Yeh, K. A. Durkin, A. Katz, *Nat. Chem.* **2010**, *2*, 1062–1068; b) J. Hassinen, P. Pulkkinen, E. Kalenius, T. Pradeep, H. Tenhu, H. Hakkinen, R. H. A. Ras, *J. Phys. Chem. Lett.* **2014**, *5*, 585–589.

[9] Z.-Y. Wang, M.-Q. Wang, Y.-L. Li, P. Luo, T.-T. Jia, R.-W. Huang, S.-Q. Zang, T. C. W. Mak, *J. Am. Chem. Soc.* **2018**, *140*, 1069–1076.

[10] Z.-J. Guan, J.-L. Zeng, Z.-A. Nan, X.-K. Wan, Y.-M. Lin, Q.-M. Wang, *Sci. Adv.* **2016**, *2*, e1600323.

[11] Z. Wang, H.-F. Su, Y.-W. Gong, Q.-P. Qu, Y.-F. Bi, C.-H. Tung, D. Sun, L.-S. Zheng, *Nat. Commun.* **2020**, *11*, 308.

[12] Deposition Number 2133430 (for **Ag155**) contains the supplementary crystallographic data for this paper. These data are provided free of charge by the joint Cambridge Crystallographic Data Centre and Fachinformationszentrum Karlsruhe Access Structures service.

[13] a) K. Nakamoto, *Infrared and Raman spectra of inorganic and coordination compounds*, John Wiley&Sons, **2009**; b) B. J. M. Rajkumar, V. Ramakrishnan, *J. Raman Spectrosc.* **2000**, *31*, 1107–1112.

[14] a) A. Desireddy, B. E. Conn, J. Guo, B. Yoon, R. N. Barnett, B. M. Monahan, K. Kirschbaum, W. P. Griffith, R. L. Whetten, U. Landman, T. P. Bigioni, *Nature* **2013**, *501*, 399–402; b) J. Yan, H. Su, H. Yang, S. Malola, S. Lin, H. Haekkinen, N. Zheng, *J. Am. Chem. Soc.* **2015**, *137*, 11880–11883.

[15] a) F. Hu, J.-J. Li, Z.-J. Guan, S.-F. Yuan, Q.-M. Wang, *Angew. Chem. Int. Ed.* **2020**, *59*, 5312–5315; *Angew. Chem.* **2020**, *132*, 5350–5353; b) C. Zeng, Y. Chen, K. Kirschbaum, K. Appavoo, M. Y. Sfeir, R. Jin, *Sci. Adv.* **2015**, *1*, e1500045.

[16] J. N. W. Johnson, *Can. J. Math.* **1966**, *18*, 169–200.

[17] Z.-J. Guan, F. Hu, S.-F. Yuan, Z.-A. Nan, Y.-M. Lin, Q.-M. Wang, *Chem. Sci.* **2019**, *10*, 3360–3365.

[18] a) A. Ghosh, R.-W. Huang, B. Alamer, E. Abou-Hamad, M. N. Hedhili, O. F. Mohammed, O. M. Bakr, *ACS Mater. Lett.* **2019**, *1*, 297–302; b) S.-D. Bian, Q.-M. Wang, *Chem. Commun.* **2008**, 5586–5588.

[19] a) K. Hirata, R. Tomihara, K. Kim, K. Koyasu, T. Tsukuda, *Phys. Chem. Chem. Phys.* **2019**, *21*, 17463–17474; b) T. Chen, Q. Yao, R. R. Nasaruddin, J. Xie, *Angew. Chem. Int. Ed.* **2019**, *58*, 11967–11977; *Angew. Chem.* **2019**, *131*, 12093–12103; c) X. Kang, S. Wang, M. Zhu, *Chem. Sci.* **2018**, *9*, 3062–3068; d) X. Kang, X. Wei, S. Jin, Q. Yuan, X. Luan, Y. Pei, S. Wang, M. Zhu, R. Jin, *Proc. Natl. Acad. Sci. USA* **2019**, *116*, 18834–18840; e) P. Chakraborty, A. Baksi, E. Khatun, A. Nag, A. Ghosh, T. Pradeep, *J. Phys. Chem. C* **2017**, *121*, 10971–10981; f) C. Schenk, A. Kracke, K. Fink, A. Kubas, W. Klopper, M. Neumaier, H. Schnoeckel, A. Schnepf, *J. Am. Chem. Soc.* **2011**, *133*, 2518–2524.

[20] A. Baksi, S. R. Harvey, G. Natarajan, V. H. Wysocki, T. Pradeep, *Chem. Commun.* **2016**, *52*, 3805–3808.

[21] a) D. M. P. Mingos, Z. Y. Lin, *Chem. Phys.* **1989**, *137*, 15–24; b) B. K. Teo, S.-Y. Yang, *J. Cluster Sci.* **2015**, *26*, 1923–1941; c) M. Walter, J. Akola, O. Lopez-Acevedo, P. D. Jadzinsky, G. Calero, C. J. Ackerson, R. L. Whetten, H. Groenbeck, H. Hakkinen, *Proc. Natl. Acad. Sci. USA* **2008**, *105*, 9157–9162.

[22] a) J. U. Reveles, S. N. Khanna, P. J. Roach, A. W. Castleman, Jr., *Proc. Natl. Acad. Sci. USA* **2006**, *103*, 18405–18410; b) Z. Luo, A. W. Castleman, *Acc. Chem. Res.* **2014**, *47*, 2931–2940.

[23] a) Y. Lyu, C. Xie, S. A. Chechetka, E. Miyako, K. Pu, *J. Am. Chem. Soc.* **2016**, *138*, 9049–9052; b) F. Mao, L. Wen, C. Sun, S. Zhang, G. Wang, J. Zeng, Y. Wang, J. Ma, M. Gao, Z. Li, *ACS Nano* **2016**, *10*, 11145–11155; c) Z. Wu, C. Ji, X. Zhao, Y. Han, K. Muellen, K. Pan, M. Yin, *J. Am. Chem. Soc.* **2019**, *141*, 7385–7390.

Manuscript received: May 8, 2022
Accepted manuscript online: May 19, 2022
Version of record online: June 15, 2022